ACS APPLIED MATERIALS & INTERFACES

www.acsami.org

Research Article

Waveguide-Integrated van der Waals Heterostructure Mid-Infrared Photodetector with High Performance

Po-Liang Chen, Yueyang Chen, Tian-Yun Chang, Wei-Qing Li, Jia-Xin Li, Seokhyeong Lee, Zhuoran Fang, Mo Li, Arka Majumdar, and Chang-Hua Liu*

Cite This: https://doi.org/10.1021/acsami.2c01094

Read Online

ACCESS | Metrics & More | Article Recommendations | Supporting Information

ABSTRACT: Extending the operation wavelength of silicon photonics to the mid-infrared (mid-IR) band will significantly benefit critical application areas, including health care, astronomy, and chemical sensing. However, a major hurdle for mid-IR silicon photonics has been the lack of high-speed, high-responsivity, and low noise-equivalent power (NEP) photodetectors. Here, we demonstrate a van der Waals (vdW) heterostructure mid-IR photodetector integrated on a silicon-on-insulator (SOI) waveguide. The detector is composed of vertically stacked black phosphorus (BP)/molybdenum ditelluride ($MoTe_2$). We measured high responsivity (up to 0.85 A/W) over a 3−4 μm spectral range, indicating that waveguide-confined light could strongly interact with vdW heterostructures on top. In addition, the waveguide-integrated detector could be modulated at high speed (>10 MHz) and its switching performance shows excellent stability. These results, together with the noise analysis, indicate that the NEP of the detector is as low as 8.2 pW/Hz$^{1/2}$. This reported critical missing piece in the silicon photonic toolbox will enable the wide-spread adoption of mid-IR integrated photonic circuits.

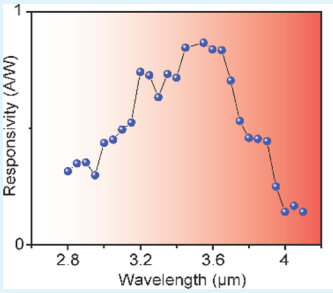

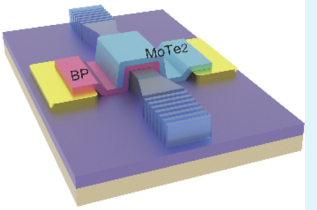

KEYWORDS: *black phosphorus, van der Waals heterostructures, photodetector, mid-infrared, silicon photonics*

1. INTRODUCTION

Thanks to compatibility with advanced complementary metal−oxide−semiconductor (CMOS) technology, large-scale photonic integrated circuits can now be readily realized in silicon. In fact, silicon photonics are already being used for optical computing and data communication in the near-infrared wavelength range,[1,2] and extending them to the mid-IR band has generated strong interest.[1,3−5] As the mid-IR wavelength band contains atmospheric transparency windows and molecular fingerprint regions, mid-IR silicon photonics could promise chip-scale spectroscopic sensing. One bottleneck to realizing mid-IR silicon photonics is the lack of a good photodetector. To that end, remarkable efforts have been devoted to integrating narrow-gap materials, such as III−V/II−VI compounds, on silicon.[1,3−6] However, the speed, responsivity, and noise-equivalent power (NEP) of these integrated photodetectors would be significantly deteriorated due to the mismatched lattice constants as well as the thermal expansions at the interfaces between silicon and mid-IR materials. As such, new materials, device architecture, and integration methods need to be adopted for high-performance chip-integrated mid-IR photodetectors.

In recent years, black phosphorus (BP) has emerged as a promising detector material in the mid-IR wavelength range, thanks to its direct and narrow band gap (~0.3 eV). BP-based detectors exhibit broad spectral photoresponses from the visible to ~4 μm mid-IR band, and their dark current levels could be orders of magnitude lower than detectors using gapless graphene.[7−11] In addition, due to the van der Waals (vdW) nature of BP, BP-based detectors can be readily transferred onto other photonic structures to form a new class of hybrid optoelectronics.[12−15] So far, numerous research works have demonstrated waveguide-integrated BP photodetectors in the near-IR (λ: 0.75−1.4 μm) or short-wavelength infrared (λ: 1.4−3 μm) regions.[10,16,17] Toward on-chip sensing applications, continued efforts further extended the detection spectrum of hybrid detectors consisting of BP phototransistors integrated with mid-IR grating couplers or photonic crystal waveguides beyond 3 μm and showed high photoresponsivity performances.[18,19] Although the light−matter interaction in such hybrid devices is along the in-plane direction and not limited by the thickness of BP, the high responsivity is mainly originated from the trap-induced photoconductive gain (i.e., photogating effect).[18−20] Furthermore, the exploitation of photogating effect could lead to low operation speed (~tens of Hz), large dark

Received: January 18, 2022
Accepted: April 16, 2022

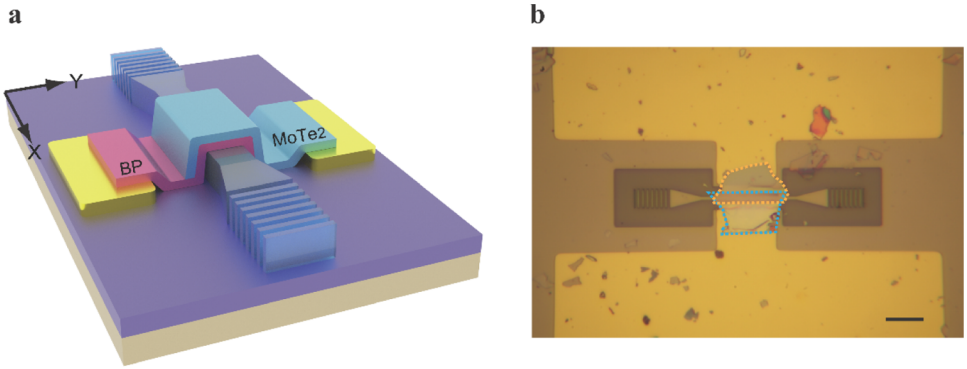

Figure 1. Device structure. (a) Schematic illustration of the hybrid photodetector composed of BP/$MoTe_2$ heterostructures integrated with a SOI waveguide. (b) Optical microscope image of the hybrid photodetector. The regions of BP and $MoTe_2$ are defined by the blue and orange dashed lines, respectively. Scale bar: 20 μm.

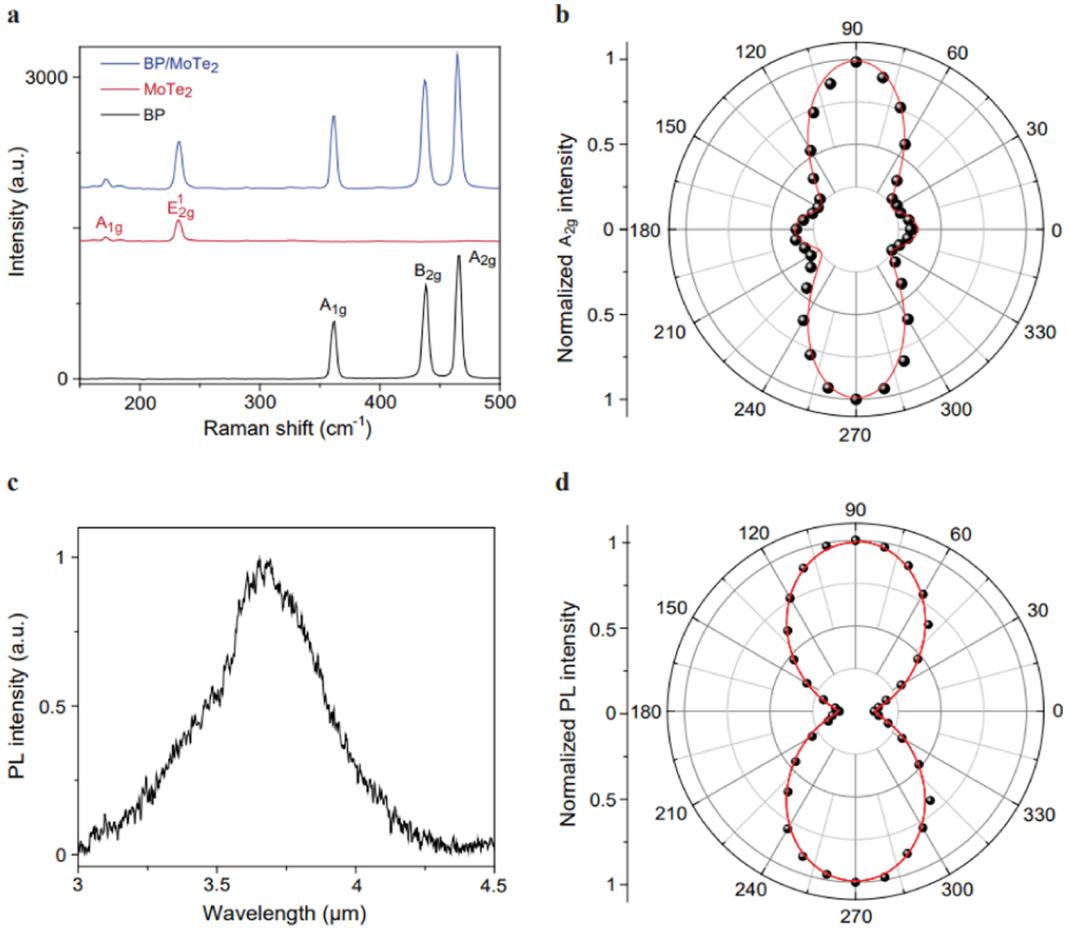

Figure 2. Raman and PL characterizations. (a) Raman spectra taken from BP (black curve), $MoTe_2$ (red curve), and BP/$MoTe_2$ heterointerfaces (blue curve), respectively. (b) Polar plot of the normalized Raman intensity of A_{2g} mode of BP as a function of rotation angle θ under parallel polarization configuration. The red line is the fitted curve to the data (black dots) using the function $a \sin^2\theta + b \cos^2\theta$. The ratio is maximum at $\theta = 90°$ (i.e., y-direction defined in Figure 1a), which indicates the armchair direction of BP is perpendicular to the propagation direction of the guided wave. (c) PL spectrum measured from the used BP flake. The excitation wavelength is 2.5 μm, and the excitation power is 250 μW. (d) Polarization-resolved PL intensity of BP. The PL is normalized with respect to the peak amplitude. The red line is the fitted curve to the data (black dots) using the function $a \sin^2\theta + b \cos^2\theta$. PL intensity is maximum at $\theta = 90°$ (i.e., *y*-direction defined in Figure 1a), which indicates the armchair direction of BP is perpendicular to the propagation direction of the guided wave.

current, and high NEP, which are not favorable for real-time and sensitive on-chip sensing applications. In this paper, we present a BP-based photodetector integrated with a mid-IR silicon waveguide. By conducting the polarization-resolved experiments, we identify the crystal orientation of BP and find that when the armchair direction of BP is aligned perpendicularly to the waveguide direction, the hybrid detector exhibits optimal performance. Our optoelectronic characterizations indicate that the demonstrated hybrid device achieves mid-IR photoresponses ranging from $\lambda = 2.8$ to 4 μm, with a peak responsivity

https://doi.org/10.1021/acsami.2c01094
ACS Appl. Mater. Interfaces XXXX, XXX, XXX−XXX

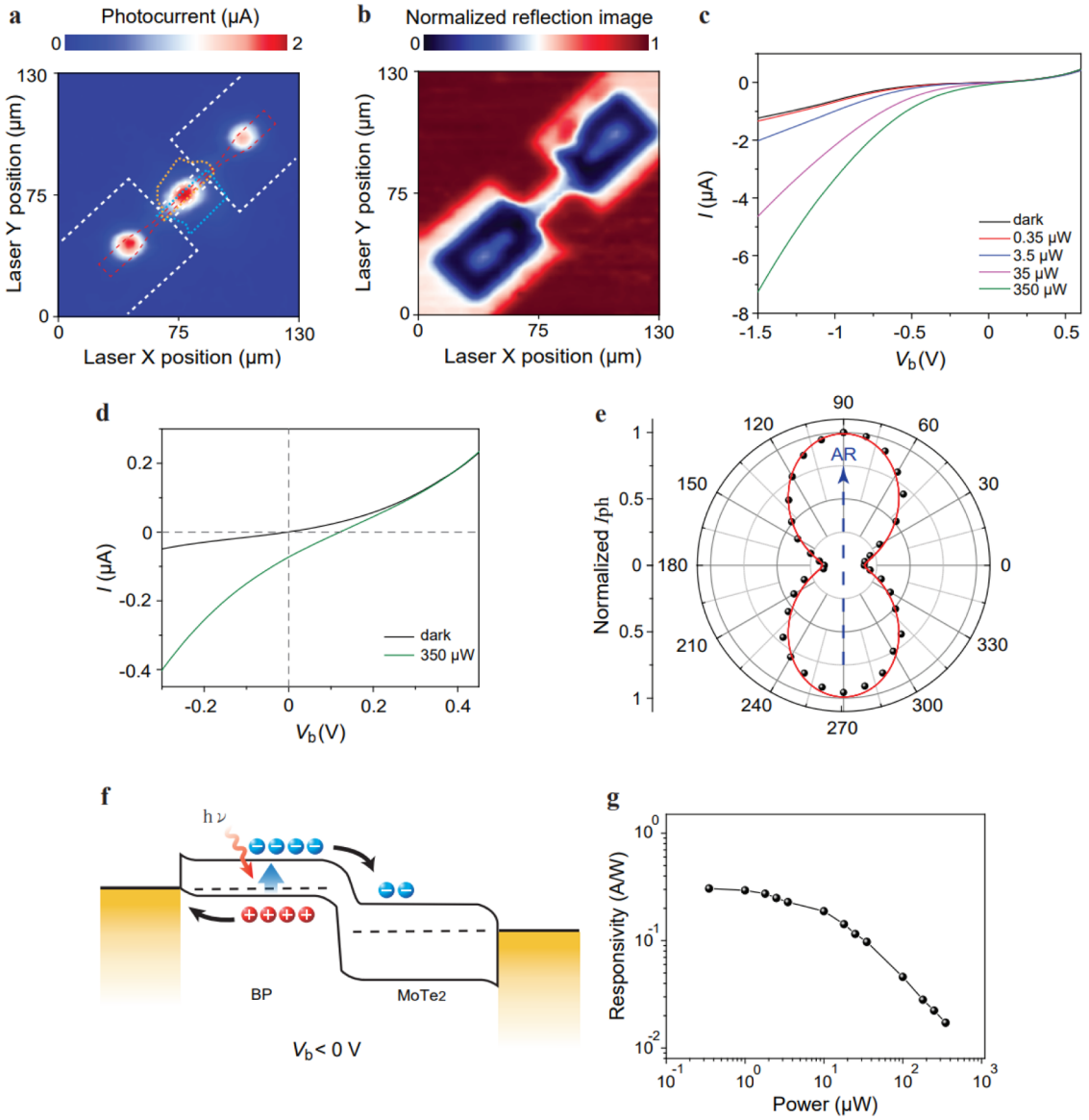

Figure 3. Scanning photocurrent and photoresponses of the BP/$MoTe_2$ photodetector. (a, b). Spatially resolved two-dimensional (a) photocurrent map and (b) reflection map (illumination wavelength: 3.7 μm). In panel (a), the regions of metal electrodes are outlined with white dashed lines and the regions of the waveguide and grating couplers are outlined with red dashed lines. The regions of BP and $MoTe_2$ are defined by the blue and orange dashed lines, respectively. (c) $I-V_b$ characteristics of the BP/$MoTe_2$ photodetector for incident laser on the heterointerface between zero and 350 μW. (d) $I-V_b$ characteristics near zero bias extracted from panel (c). (e) Measured short-circuit photocurrent generation as a function of linear polarization angle of incident laser. The photocurrent is normalized with respect to the peak amplitude. The red line is the fitted curve to the data (black dots) using the function $a \sin^2\theta + b \cos^2\theta$. $\theta = 90°$ corresponds to the y-direction, defined in Figure 1a. (f) Schematic of band diagram and transport of photocarriers under light illumination. (g) Measured photoresponsivity at $V_b = -1.5$ V versus illumination power.

~0.85 A/W. In addition, the detector exhibits fast rise (30 ns) and decay (58 ns) times and the NEP of the device was measured to be 8.2 pW/$Hz^{1/2}$ at room temperature.

2. RESULTS AND DISCUSSION

Figure 1a,b presents the schematic and optical image of the on-chip detector. The silicon waveguide and grating couplers, fabricated on a SOI substrate with a 600 nm silicon layer and 2 μm buried oxide layer, are designed to support the transverse electric (TE) mode. The photodetector is composed of the vertically stacked BP/$MoTe_2$ vdW heterostructures, which were integrated onto the silicon waveguide via the traditional dry transfer technique.[21] The Raman spectra of the transferred vdW heterostructures were measured under 532 nm excitation. The characteristics of phonon modes of BP, A_{1g} at 362.1 cm^{-1}, B_{2g} at 438.3 cm^{-1}, and A_{2g} at 466.3 cm^{-1}, can be identified (Figure 2a).[22] The Raman spectrum measured from the $MoTe_2$ region shows two modes A_{1g} at 171.2 cm^{-1}, and E^1_{2g} at 232 cm^{-1}, consistent with the literature (Figure 2a).[23] In the heterojunction region, the Raman spectrum shows prominent modes of BP and $MoTe_2$, indicating the existence of two different materials. When fabricating the device, we used the standard mechanical exfoliation method to obtain the vdW flakes. The thicknesses of BP and $MoTe_2$ flakes are 25 and 32 nm, respectively, identified by the atomic force microscopy (AFM) measurements (Figure S1, Supporting Information). Furthermore, we conducted all exfoliation as well as transfer processes in a nitrogen-filled glovebox (<0.5 ppm) to prevent the oxidation

https://doi.org/10.1021/acsami.2c01094
ACS Appl. Mater. Interfaces XXXX, XXX, XXX−XXX

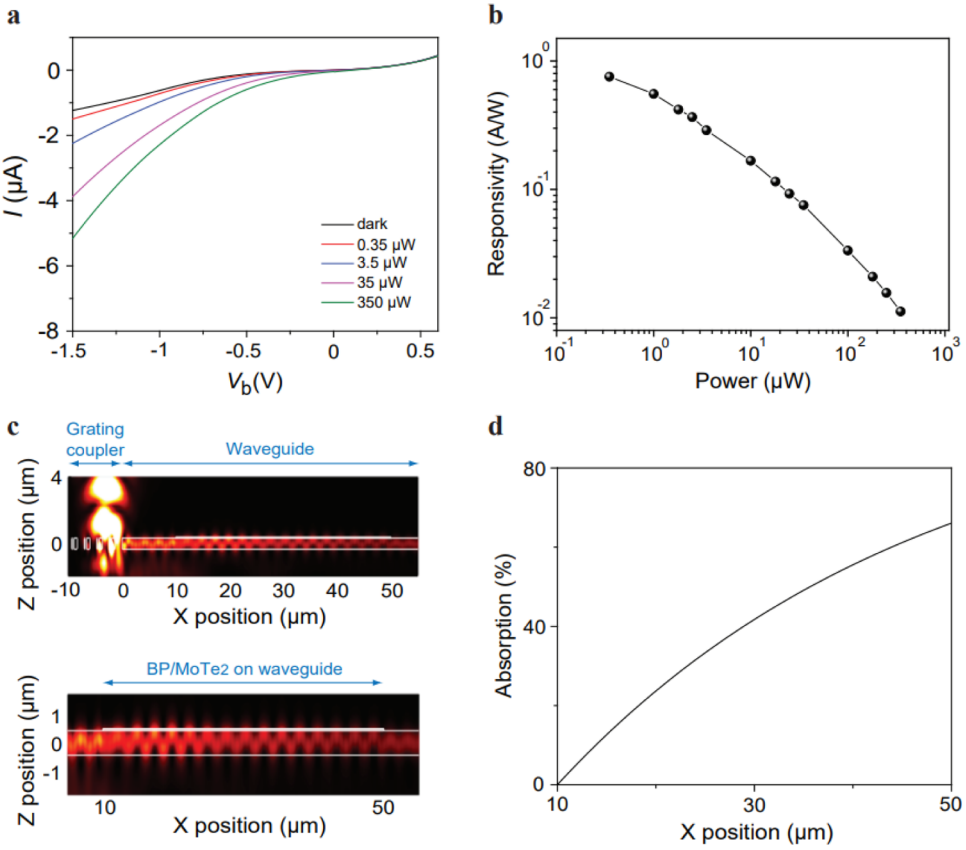

Figure 4. Photocurrent responses and FDTD simulations of the waveguide-integrated photodetector. (a) $I-V_b$ characteristics of the hybrid photodetector. The incident laser (λ = 3.7 μm) was focused on the left grating coupler, with power varying from zero to 350 μW. (b) Measured photoresponsivity at V_b = −1.5 V versus illumination power. (c) Top panel: FDTD simulation of focused mid-IR light (λ = 3.7 μm) that is coupled into the silicon waveguide. Bottom panel: zoom-in view of the region where BP/$MoTe_2$ heterostructures are stacked with the waveguide. In this simulation, we assume the thicknesses of BP and $MoTe_2$ layers are 25 and 32 nm, respectively. (d) FDTD simulation of guided light that is absorbed by the stacked BP/$MoTe_2$ heterostructures. The x position between 10 and 50 μm corresponds to the region where BP/$MoTe_2$ heterostructures are stacked with the waveguide, as defined in panel (c).

of BP and $MoTe_2$. During the transfer process, the BP and $MoTe_2$ were aligned to contact with two pre-patterned Cr/Au (5/40 nm) electrodes, respectively. The BP flake was directly attached to the silicon waveguide so that it could effectively absorb the evanescent field of the guided TE mode of the waveguide. The generated electron−hole pairs in BP could then be dissociated at the BP/$MoTe_2$ heterointerface, leading to the generation of photocurrents. Additionally, it is notable that BP exhibits strong directional absorption and transport properties due to its anisotropic in-plane lattice structure.[7−9,24,25] To maximize the interaction between BP and guided TE wave and facilitate the transport of photocarriers to metal contacts, we exploited the polarization-resolved Raman spectroscopy (Figure 2b) as well as photoluminescence measurements (Figure 2c,d) to identify the BP crystal orientation[18,22,26−28] and ensured that the armchair direction of the transferred BP was aligned perpendicularly to the propagation direction of the guided wave.

Following this, we performed scanning photocurrent microscopy[11,29,30] to spatially resolve the photoresponses of waveguide-integrated BP/$MoTe_2$ photodetector. Figure 3a shows the scanning photocurrent image derived by scanning a focused laser beam (λ = 3.7 μm, 10 μW) across the entire photonic structure and biasing the BP/$MoTe_2$ heterostructures at −1 V with $MoTe_2$ grounded. The incident light was focused to ∼8 μm (Figure S2, Supporting Information) by a zinc selenide aspheric lens (NA = 0.67), and the study was conducted at room temperature and under a vacuum of 10^{-4} Torr unless otherwise specified. Notably, the scanning photocurrent image reveals three bright spots. By comparing this image with the scanning reflection image (Figure 3b), it is clear the central bright spot comes from directly illuminating the BP/$MoTe_2$ heterostructures. The extra spots on two sides are obtained by illuminating the regions of grating couplers. Such a result indicates these in-plane couplers can couple the light from free space into the silicon waveguide. The guided light then propagates to the heterostructure photodetector and effectively interacts with the stacked BP flake through the evanescent field. We find that these two extra spots show slightly different photocurrent amplitude. This suggests the larger coupling loss or scattering loss for the light coupled from the right side of the grating coupler. This is likely because the residue was accidentally left on the right side of the grating coupler during the process of transferring vdW flakes that comprises its coupling efficiency. In addition, we note these two extra spots would become negligible if the armchair direction of BP is aligned parallelly to the propagation direction of the guided TE wave (Figures S3 and S4, Supporting Information). This evidently confirms the performance of the hybrid detector strongly depends on the crystal orientation of BP with respect to the waveguide.

We then focused on characterizing the photoresponses of vdW heterostructure detector by illuminating the mid-IR light onto the BP/$MoTe_2$ heterointerface. Figure 3c shows the

https://doi.org/10.1021/acsami.2c01094
ACS Appl. Mater. Interfaces XXXX, XXX, XXX−XXX

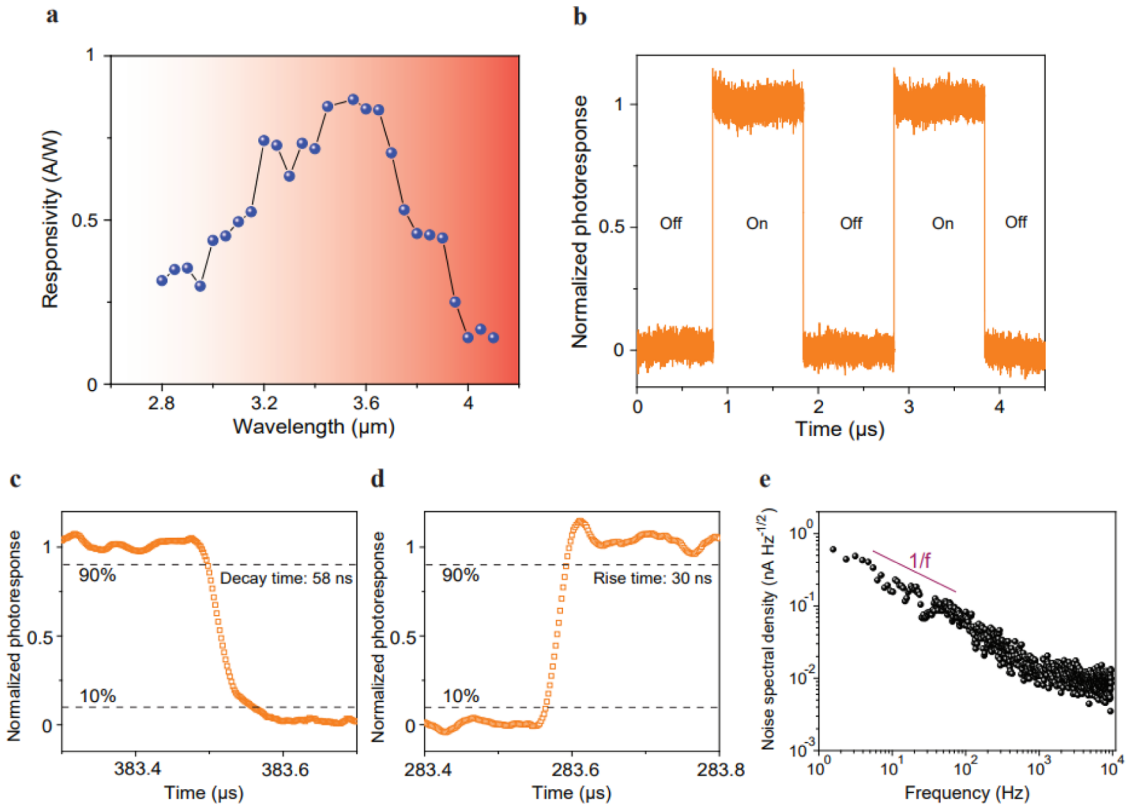

Figure 5. Spectral photoresponse, temporal photoresponse, and noise characterization. (a) Spectral-dependent responsivity of the waveguide-integrated photodetector. (b) Temporal photoresponse of the waveguide-integrated photodetector when the incident light intensity (λ = 3.7 μm, 600 μW) was modulated at a frequency of 500 kHz. Analysis of the (c) 90−10% fall time and (d) 10−90% rise time. (e) Noise spectral density measured from the waveguide-integrated photodetector.

measured $I-V$ characteristics of the photodetector. Without any illumination, we obtain the expected rectifying $I-V$ curve. This is correlated with the type II band offset formed at BP/$MoTe_2$ heterointerface (Figure S5, Supporting Information). Under light illumination (λ = 3.7 μm, linearly polarized along the armchair direction of BP), it is obvious that the open-circuit voltage and short-circuit current increase with the excitation power, exhibiting photovoltaic characteristics (Figure 3c,d). We note that the measured amplitude of short-circuit photocurrent would vary with the linear polarization angle of incident light (Figure 3e). The exhibited polarization angle-dependent variations agree with the photoluminescence and Raman measurements, as shown in Figure 2b−d, confirming that the incident mid-IR light is absorbed by BP. Moreover, when the heterointerface is subjected to a reverse bias (Figure 3c,d), the amplitude of photocurrent ($I_{ph} = I_{light} - I_{dark}$) increases dramatically with the applied bias. This suggests the bias-induced band bending not only leads to the more efficient dissociation of photoexcited electron−hole pairs at the BP/$MoTe_2$ heterointerface but also facilitates the drift of dissociated photocarriers to the metal contacts (Figure 3f). To further quantify the photoresponses, the power dependence of photoresponsivity of the BP/$MoTe_2$ detector was measured. As illustrated in Figure 3g, the responsivity of the detector can reach 0.3 A/W at low excitation power and gradually decreases with increasing excitation power due to the absorption saturation as well as the increased photocarrier recombination rate of BP. Similar behavior of power-dependent responsivity was also observed from other photodetectors based on vdW thin films.[11,31,32]

Next, we characterized the photoresponses of waveguide-integrated BP/$MoTe_2$ photodetector by illuminating the focused mid-infrared light (λ = 3.7 μm) onto the left grating coupler. The incident light was linearly polarized along the y-direction (defined in Figure 1a) to maximize the coupling efficiency of in-plane grating coupler. Figure 4a shows the $I-V$ characteristics of the hybrid detector over four orders of magnitude optical power. The calculated power dependence of responsivity, defined as the photocurrent divided by the incident light power on the grating coupler area, is shown in Figure 4b. Notably, the result reveals the peak responsivity of the hybrid detector can reach 0.75 A/W at low excitation power, which is higher than the photoresponses measured by directly focusing the mid-IR light onto the BP/$MoTe_2$ heterointerface (Figure 3g). However, when the excitation power on the left grating area is higher than 10 μW, the performed responsivity would decrease dramatically with the increase of the incident power. Such phenomenon suggests that the guided mid-IR light strongly interacts with BP through the in-plane evanescent-wave coupling, and thus the absorption saturation of BP occurs at a relatively low excitation power. To gain further insight, we simulated the light-BP interactions using the finite-difference time-domain (FDTD) method. Figure 4c shows the cross section of the fundamental TE field intensity of the hybrid detector. Clearly, the simulations indicate the mid-IR light can be coupled from the free space into the waveguide, and the guided light mode exhibits an evanescent field outside the surface of the waveguide. Due to the strong overlap of the evanescent field with the stacked BP flake, efficient light−matter interaction is expected. Our simulation shown in Figure 4d

https://doi.org/10.1021/acsami.2c01094
ACS Appl. Mater. Interfaces XXXX, XXX, XXX−XXX

reveals nearly 66% of the guided TE light could be absorbed when it propagates through the region, where the 40-μm-long BP/$MoTe_2$ heterostructures are overlaid with the waveguide. This amount of light absorption is considerably larger than the free-space absorption of the used BP (~20%).[20]

To gain further insight, we examined the spectral dependence of the hybrid detector. In this experiment, we tuned the wavelength of incident light from 2.8 to 4.1 μm. The incident light was linearly polarized along the y-direction (defined in Figure 1a) and focused onto the left grating coupler. Figure 5a demonstrates the spectral response of the detector with the excitation power fixed at 350 nW. The result clearly shows the device could exhibit photoresponsivity higher than 0.4 A/W over a broad spectral bandwidth ranging from 3 to 3.9 μm. Moreover, at λ = 3.5−3.6 μm, the performed responsivity peaks to ~0.85 A/W. This is because the silicon grating coupler exhibits the largest coupling efficiency at this wavelength region. Above λ = 3.9 μm and below λ = 3 μm, the photoresponsivity dramatically decreases, related to both the cutoff wavelength of BP absorption (~λ = 4 μm) and the grating coupler efficiency.

We finally measured the operation speed of the waveguide-integrated BP/$MoTe_2$ photodetector (see Methods). Figure 5b shows the switching behavior of the hybrid detector when the intensity of guided light (λ = 3.7 μm) was modulated on/off at 0.5 MHz using an acousto-optic modulator (AOM). Notably, our device exhibits a repeatable and stable mid-IR photoresponse, as the variations of currents in the light-on and dark states are both less than 10%. Figure 5c,d shows the analysis of transient photocurrent response. The resolved 10−90% rise time and 90−10% decay time are ~30 and ~58 ns, respectively. We note that these response times are limited by the acousto-optic beam transit time, and thus, the bandwidth of the detector could be higher than 10 MHz. Critically, these features are superior to other mid-IR waveguide-integrated BP phototransistors, which typically suffer from poor reproducibility and slow modulation speed.[18,19]

Finally, we analyzed the noise spectral density (NSD) and noise-equivalent power (NEP) of the hybrid photodetector. To characterize the NSD, we measured its dark current noise in the time domain, with the detector biased at −1.5 V. The measured discrete-time noise signal was then converted into the frequency domain by fast Fourier transform of the autocorrelation function.[29] As shown in Figure 5e, the device exhibits $1/f$ dependence of NSD in the low-frequency range, as indicated by the red line. At frequencies higher than 1 kHz, the NSD appears to be frequency independent, as the dominant noise sources are originated from the shot and thermal noises. With this analysis, the NEP of the detector, the metric that quantifies the sensitivity of the detector, can be calculated by dividing the NSD by responsivity. Critically, as the speed of our detector could reach 10 MHz, it could be operated at the minimum level of NSD (~7 pA/$\sqrt{\text{Hz}}$). This, together with its high responsivity of ~0.85 A/W, yields the NEP ~8.2 pW/$\sqrt{\text{Hz}}$ within a 1 Hz bandwidth (Δf) and detectivity D^* ~ 1.2×10^8 cm $\text{Hz}^{1/2}\text{W}^{-1}$, given that the detection area is ~100 μm^2. We note that the previously reported BP phototransistors integrated with mid-IR waveguides exhibited higher responsivity, which emanates from the effect of long-lived trapped charges.[18,19] These charge trapping and de-trapping processes could limit the operation speed of phototransistors and thus cause the devices to suffer from the low-frequency $1/f$ noise.

3. CONCLUSIONS

In summary, we demonstrate an on-chip mid-IR photodetector composed of the vdW heterostructures integrated on a SOI waveguide. Due to the strong light−matter interaction between the guided light and BP, as well as the effective and quick dissociation of the photoexcited electron−hole pairs at the BP/$MoTe_2$ heterointerface, we can simultaneously achieve high responsivity, high speed, and low NEP at room temperature, showing great promise for real-time and sensitive on-chip sensing. VdW material engineering and fabrication optimization could further enhance the performance of the device. For instance, air-stable hybrid detectors can be made via replacing BP with tellurium and the dark current of the detector can be suppressed by incorporating unipolar barriers into vdW heterostructures.[33,34] The cutoff wavelength of the hybrid detector can extend up to 8 μm by integrating the narrow-gap arsenic- or carbon-doped black phosphorus with silicon waveguides.[35−38] In addition, integrating the thicker BP flake might further increase the absorption of the evanescent field and thus enhance the responsivity of the hybrid detector, but such an approach might also lead to a higher noise level.[10,18,19] Alternatively, higher responsivity can be achieved by increasing the optical field at the surface of the waveguide via further reducing the thickness of the waveguide[39] or exploiting the advanced waveguide structures, such as the slot-waveguide and slow-waveguide designs.[40−42] It is also noteworthy that several works have already demonstrated waveguide-integrated BP modulators and BP light-emitting diodes.[15,22,27,43] These, together with our results, could constitute an important step forward in employing BP-based vdW heterostructures for the mid-infrared silicon photonics.

4. EXPERIMENTAL SECTION

4.1. Light Sources and Power Calibrations. The mid-IR light was either provided by a quantum cascade laser or by a wavelength-tunable optical parametric oscillator (OPO). The generated optical powers were measured by a thermal power sensor (Thorlabs S401C) and by an InSb detector (Infrared Associates, IS-2.0). When conducting the mid-IR scanning reflection experiments, we used the InSb detector to collect the mid-IR light reflected from our devices.

4.2. Temporal Photoresponse Measurement. To calibrate the transient rise and decay time of the photodetector, we sent the mid-IR light into an acousto-optic modulator (AOM, Isomet M1210) to switch its light intensity on and off. The modulated mid-IR light was passed through a half-waveplate and a linear polarizer to control its polarization orientation and was then focused onto the grating coupler region using a zinc selenide aspheric lens. The mid-IR light coupled into the silicon waveguide would then be detected by the integrated BP/$MoTe_2$ photodetector, leading to the photocurrent generation. We used a high-speed transimpedance amplifier to convert this photocurrent into a photovoltage signal and resolved this time-varying photoresponse using a real-time oscilloscope.

■ ASSOCIATED CONTENT

Supporting Information

The Supporting Information is available free of charge at https://pubs.acs.org/doi/10.1021/acsami.2c01094.

Detailed atomic force microscopy characterizations, characterization of the focused laser spot size, photoresponse of the hybrid photodetector, and analysis of short-circuit photoresponse (PDF)

https://doi.org/10.1021/acsami.2c01094
ACS Appl. Mater. Interfaces XXXX, XXX, XXX−XXX

AUTHOR INFORMATION

Corresponding Author

Chang-Hua Liu − *Institute of Photonics Technologies, National Tsing Hua University, Hsinchu 30013, Taiwan; Department of Electrical Engineering, National Tsing Hua University, Hsinchu 30013, Taiwan;* orcid.org/0000-0001-8042-9218; Email: changhua@gapp.nthu.edu.tw

Authors

Po-Liang Chen − *Institute of Photonics Technologies, National Tsing Hua University, Hsinchu 30013, Taiwan*

Yueyang Chen − *Department of Electrical and Computer Engineering, University of Washington, Seattle, Washington 98195, United States;* orcid.org/0000-0002-4390-550X

Tian-Yun Chang − *Institute of Photonics Technologies, National Tsing Hua University, Hsinchu 30013, Taiwan*

Wei-Qing Li − *Institute of Photonics Technologies, National Tsing Hua University, Hsinchu 30013, Taiwan*

Jia-Xin Li − *Institute of Photonics Technologies, National Tsing Hua University, Hsinchu 30013, Taiwan*

Seokhyeong Lee − *Department of Electrical and Computer Engineering, University of Washington, Seattle, Washington 98195, United States*

Zhuoran Fang − *Department of Electrical and Computer Engineering, University of Washington, Seattle, Washington 98195, United States;* orcid.org/0000-0001-8724-6633

Mo Li − *Department of Electrical and Computer Engineering, University of Washington, Seattle, Washington 98195, United States; Department of Physics, University of Washington, Seattle, Washington 98195, United States;* orcid.org/0000-0002-5500-0900

Arka Majumdar − *Department of Electrical and Computer Engineering, University of Washington, Seattle, Washington 98195, United States; Department of Physics, University of Washington, Seattle, Washington 98195, United States;* orcid.org/0000-0003-0917-590X

Complete contact information is available at: https://pubs.acs.org/10.1021/acsami.2c01094

Notes

The authors declare no competing financial interest.

ACKNOWLEDGMENTS

C.-H.L. acknowledges HC Photonics Corporation for assistance in setting up a tunable optical parametric oscillator (OPO). This work was supported by the Ministry of Science and Technology of Taiwan under Grants MOST 109-2112-M-007-032-MY3, MOST 110-2124-M-007-002, and NSF-1845009.

REFERENCES

(1) Thomson, D.; Zilkie, A.; Bowers, J. E.; Komljenovic, T.; Reed, G. T.; Vivien, L.; Marris-Morini, D.; Cassan, E.; Virot, L.; Fedeli, J. M.; Hartmann, J. M.; Schmid, J. H.; Xu, D. X.; Boeuf, F.; O'Brien, P.; Mashanovich, G. Z.; Nedeljkovic, M. Roadmap on silicon photonics. *J. Opt.* **2016**, *18*, No. 073003.

(2) Jalali, B.; Fathpour, S. Silicon photonics. *J. Lightwave Technol.* **2006**, *24*, 4600−4615.

(3) Soref, R. Mid-infrared photonics in silicon and germanium. *Nat. Photon.* **2010**, *4*, 495−497.

(4) Lin, H.; Luo, Z.; Gu, T.; Kimerling, L. C.; Wada, K.; Agarwal, A.; Hu, J. Mid-infrared integrated photonics on silicon: a perspective. *Nanophotonics* **2017**, *7*, 393−420.

(5) Spott, A.; Stanton, E. J.; Volet, N.; Peters, J. D.; Meyer, J. R.; Bowers, J. E. Heterogeneous Integration for Mid-infrared Silicon Photonics. *IEEE J. Sel. Top. Quantum Electron.* **2017**, *23*, 1−10.

(6) Kier, A. *Mid Infrared Semiconductor Optoelectronics*; SpringerVerlag: New York, NY, 2006.

(7) Xia, F.; Wang, H.; Jia, Y. Rediscovering black phosphorus as an anisotropic layered material for optoelectronics and electronics. *Nat. Commun.* **2014**, *5*, No. 4458.

(8) Ling, X.; Wang, H.; Huang, S. X.; Xia, F. N.; Dresselhaus, M. S. The renaissance of black phosphorus. *Proc. Natl. Acad. Sci. U.S.A.* **2015**, *112*, 4523−4530.

(9) Wang, X. M.; Lan, S. F. Optical properties of black phosphorus. *Adv. Opt. Photon.* **2016**, *8*, 618−655.

(10) Youngblood, N.; Chen, C.; Koester, S. J.; Li, M. Waveguide-integrated black phosphorus photodetector with high responsivity and low dark current. *Nat. Photon.* **2015**, *9*, 247−252.

(11) Chang, T.-Y.; Chen, P.-L.; Yan, J.-H.; Li, W.-Q.; Zhang, Y.-Y.; Luo, D.-I.; Li, J.-X.; Huang, K.-P.; Liu, C.-H. Ultra-Broadband, High Speed, and High-Quantum-Efficiency Photodetectors Based on Black Phosphorus. *ACS Appl. Mater. Interfaces* **2020**, *12*, 1201−1209.

(12) Liu, C. H.; Zheng, J. J.; Chen, Y. Y.; Fryett, T.; Majumdar, A. Van der Waals materials integrated nanophotonic devices. *Opt. Mater. Express* **2019**, *9*, 384−399.

(13) Youngblood, N.; Li, M. Integration of 2D materials on a silicon photonics platform for optoelectronics applications. *Nanophotonics* **2016**, *6*, 1205−1218.

(14) Brar, V. W.; Sherrott, M. C.; Jariwala, D. Emerging photonic architectures in two-dimensional opto-electronics. *Chem. Soc. Rev.* **2018**, *47*, 6824−6844.

(15) Li, J.; Liu, C. Y.; Chen, H. T.; Guo, J. S.; Zhang, M.; Dai, D. X. Hybrid silicon photonic devices with two-dimensional materials. *Nanophotonics* **2020**, *9*, 2295−2314.

(16) Chen, C.; Youngblood, N.; Peng, R. M.; Yoo, D.; Mohr, D. A.; Johnson, T. W.; Oh, S. H.; Li, M. Three-Dimensional Integration of Black Phosphorus Photodetector with Silicon Photonics and Nanoplasmonics. *Nano Lett.* **2017**, *17*, 985−991.

(17) Yin, Y. L.; Cao, R.; Guo, J. S.; Liu, C. Y.; Li, A.; Feng, X. L.; Wang, H. D.; Du, W.; Qadir, A.; Zhang, H.; Ma, Y. G.; Gao, S. R. R.; Xu, Y.; Shi, Y. C.; Tong, L. M.; Dai, D. X. High-Speed and High-Responsivity Hybrid Silicon/Black-Phosphorus Waveguide Photodetectors at 2 μm. *Laser Photonics Rev.* **2019**, *13*, No. 1900032.

(18) Huang, L.; Dong, B. W.; Guo, X.; Chang, Y. H.; Chen, N.; Huang, X.; Liao, W. G.; Zhu, C. X.; Wang, H.; Lee, C.; Ang, K. W. Waveguide-Integrated Black Phosphorus Photodetector for Mid-Infrared Applications. *ACS Nano* **2019**, *13*, 913−921.

(19) Ma, Y. M.; Dong, B. W.; Wei, J. X.; Chang, Y. H.; Huang, L.; Ang, K. W.; Lee, C. High-Responsivity Mid-Infrared Black Phosphorus Slow Light Waveguide Photodetector. *Adv. Opt. Mater.* **2020**, *8*, No. 2000337.

(20) Guo, Q. S.; Pospischil, A.; Bhuiyan, M.; Jiang, H.; Tian, H.; Farmer, D.; Deng, B. C.; Li, C.; Han, S. J.; Wang, H.; Xia, Q. F.; Ma, T. P.; Mueller, T.; Xia, F. N. Black Phosphorus Mid-Infrared Photodetectors with High Gain. *Nano Lett.* **2016**, *16*, 4648−4655.

(21) Liu, Y.; Weiss, N. O.; Duan, X. D.; Cheng, H. C.; Huang, Y.; Duan, X. F. Van der Waals heterostructures and devices. *Nat. Rev. Mater.* **2016**, *1*, No. 16042.

(22) Chang, T.-Y.; Chen, Y.; Luo, D.-I.; Li, J.-X.; Chen, P.-L.; Lee, S.; Fang, Z.; Li, W.-Q.; Zhang, Y.-Y.; Li, M.; Majumdar, A.; Liu, C.-H. Black phosphorus mid-infrared light emitting diodes integrated with silicon photonic waveguides. *Nano Lett.* **2020**, *20*, 6824−6830.

(23) Ruppert, C.; Aslan, O. B.; Heinz, T. F. Optical Properties and Band Gap of Single- and Few-Layer $MoTe_2$ Crystals. *Nano Lett.* **2014**, *14*, 6231−6236.

(24) Yuan, H. T.; Liu, X. G.; Afshinmanesh, F.; Li, W.; Xu, G.; Sun, J.; Lian, B.; Curto, A. G.; Ye, G. J.; Hikita, Y.; Shen, Z. X.; Zhang, S. C.; Chen, X. H.; Brongersma, M.; Hwang, H. Y.; Cui, Y. Polarization-sensitive broadband photodetector using a black phosphorus vertical p-n junction. *Nat. Nanotechnol.* **2015**, *10*, 707−713.

(25) Bullock, J.; Amani, M.; Cho, J.; Chen, Y. Z.; Ahn, G. H.; Adinolfi, V.; Shrestha, V. R.; Gao, Y.; Crozier, K. B.; Chueh, Y. L.; Javey, A. Polarization-resolved black phosphorus/molybdenum disulfide mid-wave infrared photodiodes with high detectivity at room temperature. *Nat. Photon.* **2018**, *12*, 601−607.
(26) Chen, C.; Chen, F.; Chen, X. L.; Deng, B. C.; Eng, B.; Jung, D.; Guo, Q. S.; Yuan, S. F.; Watanabe, K.; Taniguchi, T.; Lee, M. L.; Xia, F. N. Bright Mid-Infrared Photoluminescence from Thin-Film Black Phosphorus. *Nano Lett.* **2019**, *19*, 1488−1493.
(27) Zong, X.; Hu, H.; Ouyang, G.; Wang, J.; Shi, R.; Zhang, L.; Zeng, Q.; Zhu, C.; Chen, S.; Cheng, C.; Wang, B.; Zhang, H.; Liu, Z.; Huang, W.; Wang, T.; Wang, L.; Chen, X. Black phosphorus-based van der Waals heterostructures for mid-infrared light-emission applications. *Light: Sci. Appl.* **2020**, *9*, No. 114.
(28) Wang, J. J.; Rousseau, A.; Yang, M.; Low, T.; Francoeur, S.; Kena-Cohen, S. Mid-infrared Polarized Emission from Black Phosphorus Light-Emitting Diodes. *Nano Lett.* **2020**, *20*, 3651−3655.
(29) Liu, C. H.; Chang, Y. C.; Norris, T. B.; Zhong, Z. H. Graphene photodetectors with ultra-broadband and high responsivity at room temperature. *Nat. Nanotechnol.* **2014**, *9*, 273−278.
(30) Liu, C. H.; Dissanayake, N. M.; Lee, S.; Lee, K.; Zhong, Z. H. Evidence for Extraction of Photoexcited Hot Carriers from Graphene. *ACS Nano* **2012**, *6*, 7172−7176.
(31) Yu, W. J.; Liu, Y.; Zhou, H. L.; Yin, A. X.; Li, Z.; Huang, Y.; Duan, X. F. Highly efficient gate-tunable photocurrent generation in vertical heterostructures of layered materials. *Nat. Nanotechnol.* **2013**, *8*, 952−958.
(32) Britnell, L.; Ribeiro, R. M.; Eckmann, A.; Jalil, R.; Belle, B. D.; Mishchenko, A.; Kim, Y. J.; Gorbachev, R. V.; Georgiou, T.; Morozov, S. V.; Grigorenko, A. N.; Geim, A. K.; Casiraghi, C.; Castro Neto, A. H.; Novoselov, K. S. Strong Light-Matter Interactions in Heterostructures of Atomically Thin Films. *Science* **2013**, *340*, 1311−1314.
(33) Peng, M.; Xie, R. Z.; Wang, Z.; Wang, P.; Wang, F.; Ge, H. N.; Wang, Y.; Zhong, F.; Wu, P. S.; Ye, J. F.; Li, Q.; Zhang, L. L.; Ge, X.; Ye, Y.; Lei, Y. C.; Jiang, W.; Hu, Z. G.; Wu, F.; Zhou, X. H.; Miao, J. S.; Wang, J. L.; Yan, H. G.; Shan, C. X.; Dai, J. N.; Chen, C. Q.; Chen, X. S.; Lu, W.; Hu, W. D. Blackbody-sensitive room-temperature infrared photodetectors based on low-dimensional tellurium grown by chemical vapor deposition. *Sci. Adv.* **2021**, *7*, No. eabf7358.
(34) Chen, Y. F.; Wang, Y.; Wang, Z.; Gu, Y.; Ye, Y.; Chai, X. L.; Ye, J. F.; Chen, Y.; Xie, R. Z.; Zhou, Y.; Hu, Z. G.; Li, Q.; Zhang, L. L.; Wang, F.; Wang, P.; Miao, J. S.; Wang, J. L.; Chen, X. S.; Lu, W.; Zhou, P.; Hu, W. D. Unipolar barrier photodetectors based on van der Waals heterostructures. *Nat. Electron.* **2021**, *4*, 357−363.
(35) Long, M. S.; Gao, A. Y.; Wang, P.; Xia, H.; Ott, C.; Pan, C.; Fu, Y. J.; Liu, E. F.; Chen, X. S.; Lu, W.; Nilges, T.; Xu, J. B.; Wang, X. M.; Hu, W. D.; Miao, F. Room temperature high-detectivity mid-infrared photodetectors based on black arsenic phosphorus. *Sci. Adv.* **2017**, *3*, No. e1700589.
(36) Yuan, S. F.; Shen, C. F.; Deng, B. C.; Chen, X. L.; Guo, Q. S.; Ma, Y. Q.; Abbas, A.; Liu, B. L.; Haiges, R.; Ott, C.; Nilges, T.; Watanabe, K.; Taniguchi, T.; Sinai, O.; Naveh, D.; Zhou, C. W.; Xia, F. N. Air-Stable Room-Temperature Mid-Infrared Photodetectors Based on hBN/Black Arsenic Phosphorus/hBN Heterostructures. *Nano Lett.* **2018**, *18*, 3172−3179.
(37) Tan, W. C.; Huang, L.; Ng, R. J.; Wang, L.; Hasan, D. M. N.; Duffin, T. J.; Kumar, K. S.; Nijhuis, C. A.; Lee, C.; Ang, K. W. A Black Phosphorus Carbide Infrared Phototransistor. *Adv. Mater.* **2018**, *30*, No. 1705039.
(38) Amani, M.; Regan, E.; Bullock, J.; Ahn, G. H.; Javey, A. Mid-Wave Infrared Photoconductors Based on Black Phosphorus-Arsenic Alloys. *ACS Nano* **2017**, *11*, 11724−11731.
(39) Wu, Z. R.; Chen, Y. J.; Zhang, T. Y.; Shao, Z. K.; Wen, Y. H.; Xu, P. F.; Zhang, Y. F.; Yu, S. Y. Design and optimization of optical modulators based on graphene-on-silicon nitride microring resonators. *J. Opt.* **2017**, *19*, No. 045801.
(40) Wang, J. Q.; Cheng, Z. Z.; Chen, Z. F.; Wan, X.; Zhu, B. Q.; Tsang, H. K.; Shu, C.; Xu, J. B. High-responsivity graphene-on-silicon slot waveguide photodetectors. *Nanoscale* **2016**, *8*, 13206−13211.
(41) Phatak, A.; Cheng, Z. Z.; Qin, C. Y.; Goda, K. Design of electro-optic modulators based on graphene-on-silicon slot waveguides. *Opt. Lett.* **2016**, *41*, 2501−2504.
(42) Zhou, H.; Gu, T. Y.; McMillan, J. F.; Yu, M. B.; Lo, G. Q.; Kwong, D. L.; Feng, G. Y.; Zhou, S. H.; Wong, C. W. Enhanced photoresponsivity in graphene-silicon slow-light photonic crystal waveguides. *Appl. Phys. Lett.* **2016**, *108*, No. 111106.
(43) Huang, L.; Dong, B.; Yu, Z. G.; Zhou, J.; Ma, Y.; Zhang, Y.-W.; Lee, C.; Ang, K.-W. Mid-infrared modulators integrating silicon and black phosphorus photonics. *Mater. Today Adv.* **2021**, *12*, No. 100170.

https://doi.org/10.1021/acsami.2c01094
ACS Appl. Mater. Interfaces XXXX, XXX, XXX−XXX